

the summations indicate summing over both species,  $R_u$  is the universal gas constant, the mole fraction  $X$  is related to the mass fraction by  $m_\alpha X_\alpha = m Y_\alpha$  where  $m_\alpha$  is the molecular weight of pure species  $\alpha$  and the mixture molecular weight is  $m = X_n m_n + X_h m_h$ . Furthermore, the molar volume  $v$  is related to the density by  $v = m/\rho$ . The components of the Peng-Robinson parameters are provided by an appropriate set of mixing rules which vary for different state equations and may have variations even for the same state equation. In the present model we follow the recommendations of Harstad et. al. [9].

In order to ensure self-consistency, all of the thermodynamic properties of the flow should be calculated from the same EOS. For the present fluid dynamics simulations the properties of interest are the molar enthalpy ( $h$ ), the constant pressure molar heat capacity ( $C_p$ ) and the speed of sound ( $a_s$ ). Each of these properties can be obtained through various derivatives and functions of the Gibbs energy. Finally, for real fluids the speed of sound

$$a = \sqrt{\frac{1}{\rho \kappa_s}},$$

is given in terms of the isentropic compressibility

$$\kappa_s = \kappa_T - v T \alpha_v^2 / C_p,$$

which is related to the expansivity ( $\alpha_v$ ) and the isothermal compressibility ( $\kappa_T$ ) calculated from the state equation:

$$\alpha_v = -\frac{(\partial p / \partial T)_{v,X}}{v(\partial p / \partial v)_{T,X}}, \quad \kappa_T = \frac{-1}{v(\partial p / \partial v)_{T,X}}.$$

### Heat and Mass Transport

For a general fluid the diffusional fluxes for heat and mass transfer are functions of all thermodynamic variables. An assumption of linear dependencies is generally made [10] in which case the Onsager reciprocal relations define certain relationships between the various possible gradient multipliers. These relations can in fact be shown to be a consequence of time reversal invariance of the governing equations. The form of the diffusional fluxes adopted here is presented in a somewhat non-traditional form:

$$q_{j,IK} = - \left[ \lambda'_{IK} \frac{\partial T}{\partial x_j} + \alpha_{IK} R_u T \left( \frac{m}{m_h m_n} \right) \mathcal{J}'_j \right],$$

$$\mathcal{J}_j = - \left[ \mathcal{J}'_j + \frac{\alpha_{BK} Y_h Y_n \rho D}{T} \frac{\partial T}{\partial x_j} \right],$$

$$\mathcal{J}'_j = \rho D \left[ \alpha_D \frac{\partial Y_h}{\partial x_j} + \frac{Y_h Y_n}{R_u T} \left( \frac{m_h m_n}{m} \right) \left( \frac{v_{,h}}{m_h} - \frac{v_{,n}}{m_n} \right) \frac{\partial p}{\partial x_j} \right]$$

where  $q_{j,IK}$  is the Irwing-Kirkwood (IK) form of the heat flux,  $\lambda'_{IK}$  and  $\alpha_{IK}$  are the associated thermal conductivity and thermal diffusion factor (similar expressions exist for the Bearman-Kirkwood (BK) form of the

heat flux), and  $D$  is the binary diffusion coefficient. It can be shown that for a general fluid, a thermal conductivity  $\lambda$  may be defined by:

$$\lambda'_{IK} = \lambda + X_n X_h \alpha_{BK} \alpha_{IK} R_u \rho D / m,$$

such that  $\lim_{p \rightarrow 0} \lambda = \lambda_{KT}$  where  $\lambda_{KT}$  is the kinetically defined thermal conductivity. Although, relatively little information exists regarding the magnitudes or specific functional form of the two thermal diffusion factors  $\alpha_{IK}$  and  $\alpha_{BK}$ , they are related through:

$$\alpha_{IK} = \alpha_{BK} + \frac{1}{R_u T} \left( \frac{m_h m_n}{m} \right) \left( \frac{h_{,h}}{m_h} - \frac{h_{,n}}{m_n} \right).$$

These parameters represent the cross diffusional (Soret and Dufour) coefficients and are properties of the particular species pairs under consideration. The partial molar volume  $v_{,\alpha} = \partial v / \partial X_\alpha$  and the partial molar enthalpy  $h_{,\alpha} = \partial h / \partial X_\alpha$  are calculated from the equation of state and must obey the relations  $v = X_n v_{,n} + X_h v_{,h}$  and  $h = X_n h_{,n} + X_h h_{,h}$ . The mass diffusion factor  $\alpha_D$  is a thermodynamic function given by:

$$\alpha_D = 1 + X_\alpha \frac{\partial \ln(\varphi_\alpha)}{\partial X_\alpha},$$

where  $\varphi_\alpha$  are the fugacity coefficients which are related to the Gibbs energy and it is noteworthy that  $\alpha_D$  is independent of the species chosen in the evaluation. The formulation is now closed with the exception of specifying  $\mu$ ,  $\lambda$ ,  $D$  and  $\alpha_{IK}$  (or  $\alpha_{BK}$ ) and also the molar reference enthalpy of the mixture,  $h^0$  which is the enthalpy reference state chosen here to be at  $p^0 = 1 \text{ bar}$  (note that the reference heat capacity is given by  $C_p^0 = \partial h^0 / \partial T$ ).

### Diffusion Coefficients and Reference Enthalpy

In the context of a DNS simulation we are not interested in exactly matching the true diffusion coefficients along with their thermodynamic dependencies since the resulting Reynolds numbers would be far too large to resolve with realistic length scales. Even in the case of an arbitrarily small domain the Schmidt number for the liquid-like fluid heptane is too large to resolve the species fields for interesting Reynolds numbers. We therefore limit the range of thermodynamic state space which will be considered to the range  $600 \text{ K} \leq T \leq 1100 \text{ K}$ ,  $40 \text{ atm} \leq P \leq 80 \text{ atm}$  and  $0 \leq Y_h \leq 1$ . This particular region is chosen for two primary reasons: (1) The Peng-Robinson EOS was found to be highly accurate within this region when compared to a more accurate model; the relative error is in no case greater than approximately 1% for both the pressure and enthalpy predictions (this error can be larger than 25% at  $p = 60 \text{ atm}$  and  $T = 350 \text{ K}$ ). (2) The viscosity is predominantly a function of temperature alone and the non-dimensional Schmidt ( $Sc$ ) and Prandtl ( $Pr$ ) numbers are found to be predominantly functions of the

mass fraction. This leads to the relatively simplified diffusion coefficients:

$$\mu = \mu_R \left( \frac{T}{(T_1 + T_2)/2} \right)^{0.7}; \quad T \text{ in Kelvins,}$$

$$Sc = \frac{\mu}{\rho \alpha_D D} = 1.5 - Y_h, \quad Pr = \frac{\mu C_p / m}{\lambda} = \frac{Sc}{2 \exp(-3Y_h/2)},$$

where  $\mu_R$  is a reference viscosity and the reference temperatures  $T_1$  and  $T_2$  correspond to the free stream temperatures for mixing layer simulations. These relations give qualitatively correct trends such that the Schmidt number is greater than and less than unity for the proper mass fractions; however, the maximum value is 1.5 rather than 2 as observed in the more complete model. For subcritical conditions this allowed us to consider Reynolds numbers sufficiently large to capture the transition to turbulence [14]; however, here, due to the density stratification, transition to turbulence is not obtained for Reynolds numbers of the same magnitude (see below).

The thermal diffusion factors are poorly understood, particularly at high pressure. For low pressures some theory exists which suggest that  $\alpha_{BK}$  is nearly independent of the mass fraction (though it can generally be a function of  $T$ ). Here we choose a value of  $\alpha_{IK} = 0.1$  as a baseline parameter (see [7]) while noting that  $\alpha_{BK}$  is the parameter that corresponds to the kinetic limit in the limit  $p \rightarrow 0$ . Note also that the product  $\alpha_{BK} X_h X_n$  is the 'thermal diffusion ratio' which is essentially the ratio of Soret to Fickian diffusion effects. Finally, our comparisons with the more accurate state model show that the mixture reference enthalpy

$$h^0 = Y_n h_n^0 + Y_h h_h^0,$$

is well fit using

$$\frac{h_n^0}{m_n} = 656.72 (T^{1.071}), \quad \frac{h_h^0}{m_h} = 27.877 (T^{1.6414})$$

in MJ/kg units.

The set of equations described above is closed; however, because the most convenient choice of primitive variables for compressible flow simulations are the density, momentum and energy, the above state equation must be solved iteratively to get both the temperature and pressure simultaneously. In order to avoid costly iterations a highly accurate fit was obtained for the specific internal energy of the mixture ( $e_i$ ) over the entire state space of interest which is explicit in the temperature:

$$T = \left[ (T_L)^\theta + \left( \frac{e_i - e_L}{e_U - e_L} \right) \left\{ (T_U)^\theta - (T_L)^\theta \right\} \right]^{1/\theta},$$

where

$$\theta = 1.14 + 0.667 Y_h^{0.676},$$

$$e_L = e_1 + \left[ \frac{\rho - \rho_L}{\rho_U - \rho_L} \right] (e_2 - e_1),$$

$$e_U = e_3 + \left[ \frac{\rho - \rho_L}{\rho_U - \rho_L} \right] (e_4 - e_3),$$

and the upper (subscript  $U$ ) and lower (subscript  $L$ ) bounds are  $\rho_L = 8$ ,  $\rho_U = 248$ ,  $T_L = 600$  and  $T_U = 1100$  with density in  $kg/m^3$  and temperature in  $K$ . Finally, third order polynomial fits were obtained for the four remaining internal energy functions  $e_1(Y_h; T_L, \rho_L)$ ,  $e_2(Y_h; T_L, \rho_U)$ ,  $e_3(Y_h; T_U, \rho_L)$  and  $e_4(Y_h; T_U, \rho_U)$  as

$$e_k = E_0 + E_1 Y_h + E_2 Y_h^2 + E_3 Y_h^3; \quad k = 1, 2, 3, 4;$$

where the coefficients are provided in Table 2. This particular fit also achieves better than 1% maximum relative error when compared to the Peng-Robinson internal energy ( $e = h - pv$ ).

## Configuration

The basic configuration is described in detail in [8]; however, here there is only a one phase flow where the lower stream (subscript 2) is heptane and the upper stream (subscript 1) is nitrogen. The initial velocity profile and the forcing is also similar to [8]. The reference viscosity is calculated from a specified value of the flow Reynolds number

$$Re_0 = \frac{\Delta(\rho U)_0 \delta_{\omega,0}}{\mu_R},$$

where the initial mean momentum difference is  $\Delta(\rho U)_0 = \rho_1 U_1 - \rho_2 U_2$  and the free stream densities are calculated from a specified constant initial flow pressure ( $p_0$ ), composition and free stream temperature ( $T_1$  and  $T_2$ ). The free stream velocities are based on a specified convective Mach number ( $M_c$ ) which is modified here for real gases

$$U_1 = 2M_c a_1 \left[ 1 + \left( \frac{a_1}{a_2} \right) \sqrt{\frac{\rho_1 Z_1}{\rho_2 Z_2}} \right]^{-1}, \quad U_2 = -\sqrt{\frac{\rho_1 Z_1}{\rho_2 Z_2}} U_1,$$

where the compressibility  $Z = p/(\rho T R_u/m)$  indicates the deviation from ideal gas behavior.

## Results

The parametric study (see conditions on Table 3) first addresses the behavior of two-dimensional (2D) shear layers in order to explore the effect of the supercritical conditions and to determine the influence of the lack of information regarding the value of the thermal diffusion factors on mixing layer entrainment. The three-dimensional (3D) simulation is pretransitional, and its results illustrate the differences between the evolution of the mixing layer at sub- and supercritical conditions.

In many ways, supercritical shear layers can be regarded as one example of stratified mixing layers, however, in contrast to most numerically studied stratified layers [11], [12] and [13], the stratification is not induced by gravity and thus it is uncoupled from the

general concepts associated with the Richardson (measures buoyancy by vertical shear) and Froude (measures inertial forces by buoyancy) numbers which dominate discussions about stratified mixing layers. For those stratified layers, work must be done in the presence of gravity to entrain the fluid, and therefore the energy thus extracted from the flow is no longer available for entrainment. The result is a reduced growth rate after the formation of the primary rollers (spanwise vorticity), a delayed pairing (which may even be suppressed because the amount of kinetic energy that can be extracted from the free stream flow to overcome the buoyancy may be insufficient) and an increased number of ribs (streamwise vorticity) formed due to the additional instabilities locally created during roll-up of the spanwise structures. Not only the number of ribs increases, but they form earlier and their size is smaller; the combined effect is that less fluid is able to cross the opposite side of the layer resulting in the mixing being entrainment-limited. For 3D shear layers, the loss of available energy for entrainment results in less developed 'mushroom' structures in the spanwise cross-sectional planes, and less energetic small scale structures once the layer becomes transitional. The present results feature some of the aspects of gravitationally-stratified mixing layers, in particular the difficulty to attain the transitional regime for the same  $Re_0$ , but other aspects are different owing to the specifics of the transport matrix and equations of state of supercritical fluids.

Figure 1 illustrates the averaged ( $\langle \rangle$  means  $x_1$ -averaged) compressibility factor for the 2D shear layers at the end of the simulation ( $t\Delta U_0/\delta_{w,0} = 100$ ) for initial conditions relevant to practical applications: the initial temperature of the fuel (here heptane) is  $\sim 600$  K, that of nitrogen is 1000 K, and the fuel is injected close to maximum compression in Diesel engines (thus the choice of  $p_0 = 6$  MPa). The final value of  $t\Delta U_0/\delta_{w,0}$  was chosen based upon the observation of completed two pairings by  $t\Delta U_0/\delta_{w,0} = 100$ . The results show departures from both the ideal gas and the liquid/ideal-gas mixing layers since  $Z = 1$  for an ideal gas and  $Z \ll 1$  for liquids; the value of  $Z = 0.4$  is more akin to that of a dense gas. As the initial temperature of heptane is raised, the value of  $Z$  approaches that of an ideal gas.

The temporal variation of the nondimensional momentum thickness  $\delta_m/\delta_{w,0}$  is shown in Fig. 2 for all 2D layers, portraying the layer growth. As expected,  $\delta_m/\delta_{w,0}$  is similar up to the first pairing ( $t\Delta U_0/\delta_{w,0} = 25$ ) after which differences occur: for example, all lower  $T_{2,0}$  layers are thinner due to the larger heptane density (stronger stratification) which impedes entrainment. The influence of the identity and value of the thermal diffusion factors is very weak for the  $\alpha_{BK}$  values, and results in increasing layer growth with increasing  $\alpha_{IK}$  values. More important, at the end of the simulation the  $\alpha_{IK}$ -prescribed simulations feature a sustained growth, whereas the  $\alpha_{BK}$ -prescribed simulations show

a reduced growth implying that additional energy was removed from the flow.

Other aspects of interest pertinent to the 2D shear layers cannot be presented here due to space constraints, however, it is clear that supercritical shear layers behave differently from subcritical ones. To further illustrate this difference between sub- and supercritical behavior, we present in Fig. 3 contour plots of the spanwise vorticity in a plane between the braids (that connect adjacent spanwise vortex cores) of the 3D shear layer (Run 8) at  $t\Delta U_0/\delta_{w,0} = 100$ . The spanwise vorticity is often displayed to visualize the large scale rollers (i.e. the spanwise structures) in mixing layers at low  $Ma$ . Clearly, there is very little positive vorticity that has been created (all initial spanwise vorticity is negative due to the initial mean velocity profile), and since it is the occurrence of this positive spanwise vorticity that is related to the transition to turbulence, we conclude that the transitional regime has not been reached; in contrast, subcritical 3D shear layers with similar initial conditions are transitional at  $t\Delta U_0/\delta_{w,0} = 100$  [14]. This is in agreement with other cited studies of stratified mixing layers showing similar impeded transition to turbulence. The heptane mass fraction contours plotted in Fig. 4 (braid plane) and Fig. 5 (between the braids plane) displays specific nonuniformities that result from solubility effects of nitrogen into heptane and shows features similar to the threads optically identified in [5]. Additionally, the density gradient (not shown due to space constraints) plotted both in the braid and in between the braid plane shows concentrated 'wisp'-like features similar to the optically identified [5] threads that break off from a supercritical jet.

## Conclusions

A previously developed model of supercritical fluid behavior has been here adapted to the configuration of a shear layer, and Direct Numerical Simulations have been performed to investigate supercritical fluid entrainment and mixing. The results show that due to the density stratification, the growth of the layer is diminished with respect to previously studied subcritical layers, and that transition to turbulence is suppressed. Moreover, pretransitional results from 3D simulations indicate that optically identified entities breaking off from fluid jets in convective flows may contain a variety of heptane-nitrogen compositions.

## ACKNOWLEDGMENT

This research was conducted at the Jet Propulsion Laboratory. It was jointly sponsored by General Electric under the Air Force Office of Scientific Research Focussed Research Initiative with Dr. Hukam Mongia as technical contract monitor, and by the National Aeronautics and Space Administration, the Lewis Research Center with Dr. Daniel L. Bulzan as technical contract monitor. Computational resources were provided by the supercomputing facility at JPL.

## References

- [1] Hirshfelder, J. O., Curtis, C. F. and Bird, R. B., *Molecular theory of gases and liquids*, John Wiley and Sons, Inc., 1964
- [2] Prausnitz, J., Lichtenthaler, R. and de Azevedo, E., *Molecular thermodynamics for fluid-phase equilibrium*, Prentice-Hall, Inc., 1986
- [3] Mayer, W., Schik, A., Schweitzer, C. and Schaffler, M., "Injection and mixing processes in high pressure LOX/GH2 rocket combustors", AIAA 96-2620
- [4] Mayer, W., Ivancic, B., Schik, A. and Hornung, U., "Propellant atomization in LOX/GH2 rocket combustors", AIAA 98-3685
- [5] Chehroudi, B., Talley and Coy, E., "Initial growth rate and visual characteristics of a round jet into a sub- to supercritical environment of relevance to rocket, gas turbine and Diesel engines", AIAA 99-0206
- [6] Harstad, K. and Bellan, J., "Isolated fluid oxygen drop behavior in fluid hydrogen at rocket chamber pressures", *Int. J. Heat Mass Transfer*, **41**, 3537-3550, 1998
- [7] Harstad, K. and Bellan, J., "An all-pressure fluid-drop model applied to a binary mixture: heptane in nitrogen", submitted for publication, 1999
- [8] Miller, R. S. and Bellan, J., "Direct numerical simulation of a confined three-dimensional gas mixing layer with one evaporating hydrocarbon-droplet laden stream", *J. Fluid Mech.*, in print, 1999
- [9] Harstad, K. G., Miller, R. S., and Bellan, J., "Efficient high pressure state equations", *A. I. Ch. E.*, **43**(6), 1605-1610, 1997
- [10] Keizer, J., *Statistical thermodynamics of non-equilibrium processes*, Springer-Verlag, New York, 1987
- [11] Cortesi, A. B., Smith, B. L., Yadigaroglu, G. and Banerjee, S., "Numerical investigation of the entrainment and mixing processes in neutral and stably-stratified mixing layers", *Physics of Fluids*, **11**, 162-185, 1999
- [12] Briggs, D. A., Ferziger, J. H., Koseff, J. R. and Monismith, S. G., "Turbulent mixing in a shear-free stably stratified two-layer fluid", *J. Fluid Mech.*, **354**, 175-208, 1998
- [13] Maslowe, S. A. and Kelly, R. E., "Inviscid instability of an unbounded heterogeneous shear layer", *J. Fluid Mech.*, **48**(2), 405-415, 1971
- [14] Miller, R. S. and Bellan, J., "Direct numerical simulation and subgrid analysis of a transitional droplet laden mixing layer", submitted for publication, 1999

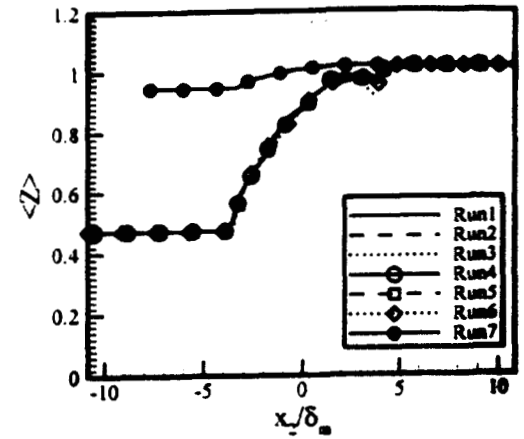


Fig. 1 Averaged compressibility factor for Runs 1-7 (see Table 3) versus the nondimensional cross stream coordinate.

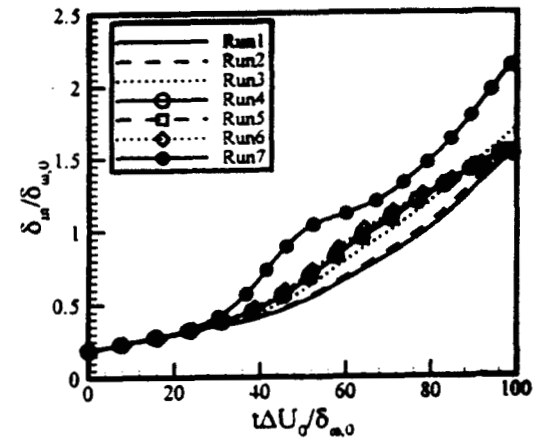


Fig. 2 Nondimensional momentum thickness versus a nondimensional time for Runs 1-7 (see Table 3)

Species	$M$ [ $\frac{kg}{kmole}$ ]	$T^*$ [K]	$T^*$ [atm]	$\nu$ [ $\frac{m^2}{kg\cdot mole}$ ]	$Z$	$\eta$
Nitrogen	28.013	126.26	33.55	0.0898	0.290	0.039
Heptane	100.205	540.3	27.04	0.432	0.263	0.349

Table 1: Pure substance properties.

energy [MJ/kg]	$E_0$	$E_1$	$E_2$	$E_3$
$e_1(Y_h, T_f, \rho_f)$	0.44142	0.51813	$1.8118 \times 10^{-3}$	$6.12810 \times 10^{-6}$
$e_2(Y_h, T_f, \rho_f)$	0.41489	0.47173	$1.4262 \times 10^{-2}$	$2.25095 \times 10^{-3}$
$e_3(Y_h, T_f, \rho_f)$	0.86090	1.78435	$1.9375 \times 10^{-3}$	$4.78990 \times 10^{-6}$
$e_4(Y_h, T_f, \rho_f)$	0.85262	1.76317	$-1.9197 \times 10^{-2}$	$2.59000 \times 10^{-3}$

Table 2: Polynomial curve fit coefficients.

Run	$T_{2,0}$ [K]	$N_1 \times N_2 (\times N_3)$	$\alpha_{IK}$	$\alpha_{BK}$
1	600	$200 \times 232$	0.1	
2	600	$200 \times 232$	1.0	
3	600	$200 \times 232$	5.0	
4	600	$200 \times 232$		0.1
5	600	$200 \times 232$		1.0
6	600	$200 \times 232$		5.0
7	900	$200 \times 232$	0.1	
8	600	$200 \times 232 \times 120$	0.1	

Table 3: Simulation parameters. All runs have 4 initial vortices and two pairings,  $M_c = 0.35$ ,  $Re_0 = 400$ ,  $T_{1,0} = 1000K$ , and  $p_0 = 6MPa$ .

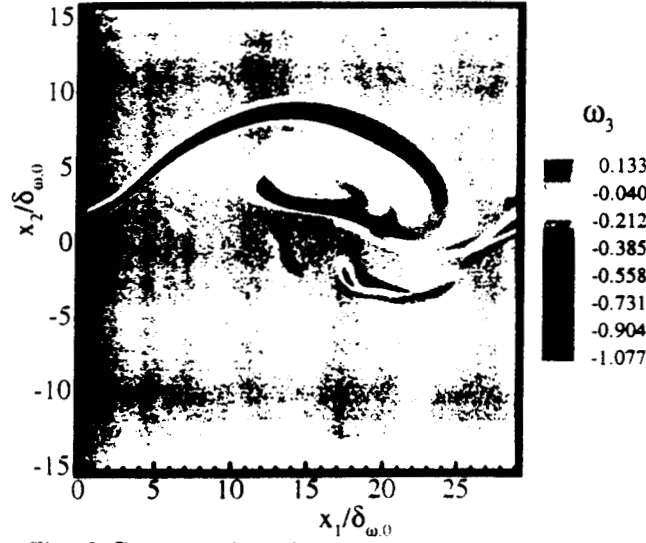


Fig. 3 Contour plot of the spanwise vorticity in a plane between the braids for the 3D Run 8 (see Table 3).

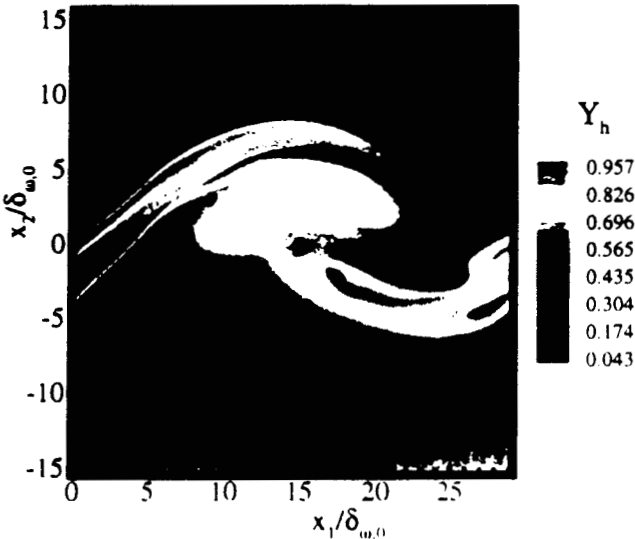


Fig. 4 Heptane mass fraction for the 3D Run 8 in a braid plane.

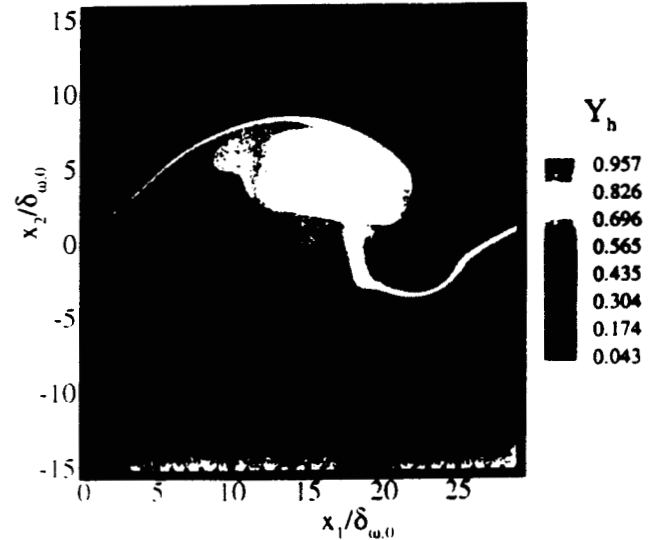


Fig. 5 Heptane mass fraction for the 3D Run 8 in a plane between the braids.